

# **A metasurface doublet for compactly and widely zooming imaging**

Yunxuan Wei<sup>1,2</sup>, Yuxi Wang<sup>1,2</sup>, Xing Feng<sup>1,2</sup>, Shunyu Xiao<sup>1</sup>, Zhaokun Wang<sup>1</sup>, Tie Hu<sup>1</sup>, Manchen Hu<sup>1</sup>, Ming Zhao<sup>1,\*</sup>, Jinsong Xia<sup>1,\*</sup>, and Zhenyu Yang<sup>1,\*</sup>

<sup>1</sup> Wuhan National Laboratory for Optoelectronics, School of Optical and Electronic Information, Huazhong University of Science and Technology (HUST), 430074, Wuhan, Hubei, China

<sup>2</sup>These authors contributed equally: Yunxuan Wei, Yuxi Wang and Xing Feng

\*Corresponding authors: zyang@hust.edu.cn, jsxia@hust.edu.cn, zhaoming@hust.edu.cn

Zooming imaging has been widely applied in cameras, cell phones, mixed reality and microscopy. Traditional zooming systems rely on the axial movement of several refractive lenses to change focal lengths, making them complex and large in scale. Metalenses make it possible to bring a revolution for zooming systems with flatness and high tunability. However, for the exiting tunable metalenses, the verified range of image zooming is no more than  $5\times$  which is insufficient for increasing requirements of large zooming power, and most of them requires extra space for moving or stretching. Here, we demonstrate a tunable metasurface doublet with a  $\pm 18\times$  tunable range of focal length as well as image zooming. With a relative rotation between two metasurfaces, the same doublet is able to work as both a positive lens and a negative lens, and a  $\pm 18\times$  focal length varying range is demonstrated without extra working space. Under the positive lens mode, the average focusing efficiency is up to 54%, and a  $18\times$  zooming imaging is also achieved. Our demonstration can meet the zooming range requirement for most optical systems, whereas with an ultrathin scale.

Zooming imaging systems have been developed for a long time, and there are many technologies to form a lens with adjustable focal length for zooming. Mechanical axial movements of several lenses are widely used in cameras and other imaging system to change their focal lengths, which requires a large working space for moving and a considerable room for the complicated lenses. Although tunable freeform lenses based on lateral displacement have been reported<sup>1-3</sup>, they are still bulky because of the use of thick refractive elements. Liquid crystal lenses with flexible adjustable focal spots are another application<sup>4-9</sup>, whereas many of them are polarization dependent. Moreover, they are also limited in the small aperture or the low numerical aperture because of the finite tunable area of refractive index<sup>7-9</sup>, or limited in the discontinuous adjustment of focal lengths<sup>4,6</sup>. Deformable lenses made of liquid or other elastic materials are small, widely tunable and high-speed<sup>10-14</sup>, but it is hard to control their whole surfaces precisely thus aberrations are increased. Metasurfaces, a kind of flat optical device consisted of arrays of subwavelength scatters, enables ultrathin and multifunctional optical elements. With the ability to control the phase, transmittance, polarization and wavevector of the incidence under a subwavelength scale, metasurfaces have been widely applied in flat lenses<sup>15-20</sup>, holograms<sup>21-25</sup>, polarization-sensitive elements<sup>26-29</sup>, beam generators<sup>30-33</sup> and tunable devices<sup>34-37</sup>. Metasurface-based lenses (Metalenses) have also showed its capability in the field of compactly tunable lenses systems. Combinations of MEMS and metalenses make it possible to change the focal length at a high speed up to kHz by axially adjusting the distance between two metalenses<sup>38</sup>, whereas they are in quite small scales (um) thus impossible to perform in those applications requiring large apertures. Metalenses based on elastic substrates are one approach to achieve flexible focal spots with adaptive focal lengths<sup>39-41</sup> and orientations<sup>41</sup>, but continuously high voltages (kv) have to be applied for generating mechanical forces to produce and keep the targeting shape and deformation<sup>41</sup>. Thermal is also used to change the index map of the thermo-optical material

assembled with metalenses as well as the accumulated phase<sup>42</sup>, but the response time significantly increases when the lens' scale enlarges. Metalenses based on Alvarez lenses concept introduce a large tunable capacity of focal length<sup>43</sup>, however parts of structures become useless during relatively shifting, which reduces the lens' aperture and efficiency. Polarization is also used to form a tunable metalense with chromatic aberration corrected<sup>44</sup>, but the polarization sensitivity is undesirable for usual image applications. Finally, most kinds of tunable metalenses above need extra space for moving or stretching when adjusting, reducing their integrated levels. Meanwhile, all of their demonstrated image zooming abilities are no more than  $5\times$ , which cannot satisfy the increasing commercial requirement of a large zooming power.

Here, we demonstrate a metasurface doublet with a large area tunable focal length, which requires no more extra working space. By rotating one of two metasurfaces of the doublet, the focal lengths can theoretically be adjusted from  $+F_0$  to infinity in a positive lens mode, whereas from  $-F_0$  to negative infinity in a negative lens mode in the other direction. Silicon and silica are used respectively for nanopillars and bases to reach a high transmittance and a full phase control in the near infrared spectrum. In this work, we experimentally achieved a  $18\times$  zoom capability along with zooming imaging, which is the largest among all types of tunable metalenses so far as we know.

**Principles of the metasurface doublet.** The operation principle of the doublet is briefly shown in Fig .1a. In order to establish the relationship between focal length and rotation, the primitive point is to construct an output wavefront from the doublet connecting with rotation. We choose the phase profile of a spherical lens as the foundation of our design but not of a focusing metalens because a larger phase error appears during the adjusting

process with the later one (see details in Supplementary Section 1). Assuming the phase profile of the first metasurface of the doublet is

$$\varphi_1(r, \theta_0) = \text{round}\left[\frac{1}{\lambda F_0} r^2\right](\theta_0 + C(r))$$

Where  $r$  and  $\theta_0$  are the coordinates in the polar geometry with the center of lenses as (0,0) and the  $x$  axis as  $(r, 0)$ ,  $\lambda$  is the operating wavelength,  $F_0$  is the original focal length. Here,  $\text{round}[]$  means to replace the number with the nearest integer, which is used to solve the discontinuity of the phase with its periodicity of  $2\pi$ .  $C(r)$  is a function with no relationship with  $\theta_0$ , which is raised for the optimization of the geometric distribution of the phase profile. In our design,  $C(r) = \frac{\pi}{12} \text{round}\left[\frac{r^2}{\lambda F_0}\right]$  is optimized purposely to enhance the circular geometric symmetry of the phase profile for reducing the impact of the distance between two metasurfaces on the focal quality. Although in the design we assume that the phase profile from the first metasurface does not change when the incidence reaches the second metasurface due to the slight distance between two metasurfaces, the phase profile actually varies during its spatial spread and introduces phase errors. With a rotational symmetry design, the phase gradient of the metasurface maps more averagely and smoothly thus the phase error from the spatial spread along with the final wavefront output from the doublet distributes circularly symmetrically. Since the geometrical symmetry of the lens is maintained, the quality of the focal spot is impacted less comparing with the none geometrical symmetry design. We demonstrate this experimentally with another pair of designed metasurface doublet without  $C(r)$  for a comparison, and results are listed in Supplementary Section 2. And assuming the phase profile of the second metasurface is

$$\varphi_2(r, \theta_0) = -\text{round}\left[\frac{1}{\lambda F_0} r^2\right](\theta_0 + C(r))$$

when the second metasurface is rotated an angle  $\theta$  and such two metasurfaces are located closely, the phase profile of the output wavefront of the doublet is

$$\varphi(r, \theta) = \varphi_1(r, \theta_0) + \varphi_2(r, \theta_0 + \theta) = -\text{round}\left[\frac{1}{\lambda F_0} r^2\right] \theta$$

Meantime, the phase profile of a spherical lens is  $\varphi_0(r) = -\left(\frac{1}{\lambda F} r^2\right) \pi$ . Comparing  $\varphi(r, \theta)$  and  $\varphi_0(r)$ , we find  $\varphi(r, \theta)$  shown in Fig. 1b is a partly quantization of  $\varphi_0(r)$ , and the focal length is as a function of rotation angle  $\theta$

$$F(\theta) = \frac{\theta}{\pi} F_0$$

where  $F$  is the focal length of the doublet, and  $k = \frac{\theta}{\pi}$  is the zoom power of the doublet. Such a quantization brings a decrease of diffraction efficiency. According to multilevel diffractive lenses<sup>45</sup>, when the number of quantitative levels among  $2\pi$  is  $n = 2\pi/\theta$ , the diffraction efficiency is  $\eta_n = (\text{sinc}(1/n))^2$ . Typically, the diffraction efficiency is 40.5% when  $\theta = \pi$  ( $1 \times$ ), 81.1% when  $\theta = \pi/2$  ( $2 \times$ ) and 95.0% when  $\theta = \pi/4$  ( $4 \times$ ). The diffraction efficiency increases when  $F$  grows, so a minimal focal length larger than  $F_0$  can be chosen for a higher average diffraction efficiency if necessary.

In this work, we design the metasurface doublet at a wavelength of 1550 nm. The unit scatter of the metasurface shown in Fig. 2a consists of a silicon cylinder arranged on a silica square lattice. The spatial rotational symmetry of the scatter ensures that it is polarization insensitive. Silicon and silica are chosen to form a high-contrast index condition and for their high transmittance in near infrared wavelengths. The light field response of the nano scatter is numerically simulated and optimized with finite-difference time-domain (FDTD) approach. Since the incident comes from different sides for two metasurfaces of the doublet, we simulate in two conditions with the light injects from the bottom or the top of the scatter. The optimization is set with three rules. Firstly, a high transmittance and a full phase control are

reached with varying radius  $R$ . Secondly, the response of the nano scatter relies weakly on the incident angle to perform well under oblique incidences since the light injects from different orientations under most practical occasions. Thirdly, both conditions above are achieved for the incidence from both the bottom and the top of the nano scatter. Finally, the lattice constant is set to  $P = 600$  nm and the height of the silicon cylinder is  $H = 700$  nm. The transmittance and phase shift of the nano scatter versus the radius of the silicon cylinder  $R$  under a normal incidence from different sides of the scatter are shown in Fig.2 a, and such responses under different incident angles are plotted in Fig. 2b,c. With the radius  $R$  varying continuously from 60 nm to 260 nm, a nearly  $2\pi$  phase shift and a transmittance above 80% is achieved for a normal incidence. Furthermore, most of nano scatters in the radius band show a high tolerance for the oblique incidence.

**Focusing with the metasurface doublet.** To experimentally demonstrate our design, we fabricated a metasurface doublet with a diameter of 1 mm and a minimal focal length of 3 mm. Detail of fabrication of the doublet and the designed phase profiles of two metasurfaces are shown in Supplementary Section 3 and Supplementary Fig. 4. Optical micrographs of two fabricated metasurfaces and two scanning electron micrographs for one of them are shown in Fig. 2d and Fig. 2e,f. A SiO<sub>2</sub> layer with a thickness of about 2.5  $\mu$ m was deposited on both metasurfaces outer the nano structures to protect the nano scatters from being scratched. A round of calibrations with marks was also carved around the nano structures for rotation alignment. The focusing behavior of the metalens was measured under a collimated 1550 nm illumination (the detail of the experimental setup is listed in Supplementary Fig. 5 and Supplementary Fig. 6).

Figure 3a depicts the normalized intensity of focal fields of the  $xz$  plane and the focal plane under six chosen rotation angles with the focal length changing from 3 mm to 54 mm

along with the zooming power adjusted from  $1\times$  to  $18\times$ . The NA of the doublet varies from 0.164 to 0.001. At each rotation angle, the position of the focal plane fits well with the designed focal length. The depth and the size of the focus extends when the focal length increase, responding to the drop of NA. Supplementary Video 1 shows the focusing behavior at a rotation angle of  $90^\circ$ . We also collected the focal length under both positive and negative lens mode per  $10^\circ$  of rotation angle in Fig. 3b. The averagely shift of the focal length from the theory is 1.7%, which indicates an excellent match between experiment and design. Note that the deviation of the focal length is mainly from the rotation alignment error at each angle. Although we measured the focal length of the doublet under negative lens mode indirectly by testing a positive focal length system comprising the doublet and a conventional lens and then calculating for the doublet, it is hard to define or measure the focusing efficiency and FWHM (full width half maximum) of a single negative lens even when it is combined with other lenses. Therefore, we only tested the focusing efficiency and FWHM under positive lens mode in Fig. 3c. The focal efficiency is defined as the power gathered in a circular area with a diameter of  $2\times\text{FWHM}$  to the total power in a circular area with a diameter of 1 mm in the focal plane. The center of both circular areas is the point of the maximum intensity. The tested FWHM is averagely 27% larger than the diffraction limit ( $\frac{0.514\lambda}{NA}$ ). Under the rotation angle of  $10^\circ$ , the FWHM is 60% larger than the diffractive limit, resulting from a weak focusing behavior with a small NA (0.001). As for the focusing efficiency, it appears a minimum of 23% in  $180^\circ$  with a minimal focal length of 3 mm and gently increases to 82% in  $10^\circ$  with a focal length of 54 mm. The rotation-angle-depending quantitative focusing phase profile results in such relationship between the focusing efficiency and the rotation angle. The average focusing efficiency is up to 54%, less than the theoretical value of 63%. Besides the quantitation in the design, the efficiency loss largely

comes from the dislocation and the unideal distance between two metasurfaces as both of them introduce phase errors to the output phase profile of the doublet. The dislocation directly changes the phase profile function of the doublet thus interrupts the focusing behavior. Meanwhile, since the phase profile changes during its spatial spread, the wavefront reaching the second metasurface diverges increasingly significantly from the designed one when the distance between two metasurfaces becomes larger. These can be avoided with a more accurate alignment technique. Another reason of the efficiency decrease can be the unideal response of the nano scatter. Firstly, fabrication errors surely bring imperfect shapes and sizes of nano scatters, which straightly cause the distinction of performance between the fabricated doublet and the designed one. Secondly, although optimized, the phase shift and the transmittance response of some of nano scatters still relies on the incident angle relatively strongly in Fig. 2b,c. However, after the modulation of the first metasurface, the incident plane wave is obviously diffracted into different orientations before injecting into the second one, leading to a spatial-varying deviation between the real wavefront response and the desired ones. Finally, nano scatters are arranged roundly but not strictly following their lattice periods, which somehow disturbs their wavefront responses. Such divergencies of phase and transmittance surely impact the final wavefront output of the doublet, thus reducing the efficiency.

**Imaging with the metasurface doublet.** We also experimentally characterized the zooming imaging ability of the metasurface doublet. A  $4f$  system consisted of a metasurface doublet and a conventional lens with a focal length of 200 mm is set for the imaging experiment (see Supplementary Fig. 7 for details of imaging testing setups). Note that the reducing of the  $4f$  system is so significant that many parts of a standard United States Air Force target are too close to or under the resolution limit of the imaging system, so we



fabricated a designed resolution target for test (for details of an image of the standard United States Air Force target and the parameters of the fabricated resolution target, see Supplementary Fig. 8 and Supplementary Fig.9). The desired width of the narrowest target line's image is about  $2.3 \times \text{FWHM}$  of the focal spot under the rotation angle of  $180^\circ$ . Note that the slenderest part of the logo 'HUST' is still close to the diffraction limit, so it would be dimmer than other areas. The zooming image was recorded under the rotation angle of  $10^\circ$ ,  $20^\circ$ ,  $30^\circ$ ,  $50^\circ$ ,  $90^\circ$  and  $180^\circ$ , representing the zooming power of  $18 \times$ ,  $9 \times$ ,  $6 \times$ ,  $3.6 \times$ ,  $2 \times$  and  $1 \times$ . In order to avoid the light going through the area outer the doublet and increase the contrast, the whole target was divided into several small parts with an aperture and captured respectively. Images after reconstruction are listed in Figs. 4a-4f. Note that the diffraction limits of the doublet and the magnification power enlarge together when zooming, so the resolution of the system only varies slightly. We also magnified the images of  $180^\circ$ ,  $90^\circ$  and  $50^\circ$  to the same ideal magnification of  $9 \times$  in Figs. 4g-4h, and all of them are clearly imaged with approximately the same sizes. According to our experimental results, the resolution target is clearly distinguished under all of six rotation angles with corresponding zoom power, indicating that a total zoom range of  $18 \times$  is achieved.

**Conclusion.** In summary, we have introduced and verified a metasurface doublet with rotationally varying focal length for large range zooming imaging. By rotating from  $180^\circ$  to  $10^\circ$ , the focal length is adjusted from 3 mm to 54 mm, whereas from -3 mm to -54 mm when rotation from  $-180^\circ$  to  $-10^\circ$ . This indicates the doublet is equipped with two modes of both a positive and a negative lens, representing to a zoom range of  $18 \times$  and  $-18 \times$ . The doublet is able to focus light closely to the diffraction limit with an average focusing efficiency of 54% without any extra working space for moving or stretching. We have also tested its imaging ability under a positive lens mode, and the results have shown that a  $18 \times$  zooming imaging

capacity is reached. The whole demonstration was finished at a wavelength of 1550 nm, but the concept can be extended to any wavelengths. With a high tunability and a compact scale, such a tunable metasurface doublet can find various applications in most occasions in need of zooming imaging, such as cameras, mixed reality and microscopy.

## **Acknowledgements**

This work was funded by the National Natural Science Foundation of China (NSFC, grant no. 61835008 and grant no. 11574102), the Fundamental Research Funds for the Central Universities (grant no. 2019kfyXKJC038), and the State Key Laboratory of Advanced Optical Communication Systems and Networks project, Shanghai Jiao Tong University, China (grant no. 2019GZKF03001). We are grateful for device fabrication support from the Center of Micro-Fabrication and Characterization (CMFC) in the Wuhan National Laboratory for Optoelectronics (WNLO) of Huazhong University of Science and Technology (HUST).

## **Author contributions**

Y.X.Wei had the original idea, conceived the study, finished the simulations; F.X. performed the measurements with the help from Y.X.Wei and S.Y.X.; Y.X.Wang fabricated the samples and analyzed them; J.S.X. supervised the fabrication; M.Z. and Z.Y.Y. supervised the work and manuscript writing. All authors discussed the results. Y.X.Wei wrote a first draft of the manuscript, which was then refined by contributions from all authors.

## Reference

- 1 Lohmann, A. W. A new class of varifocal lenses. *Applied optics* **9**, 1669-1671, doi:10.1364/ao.9.001669 (1970).
- 2 Zou, Y., Zhang, W., Chau, F. S. & Zhou, G. Miniature adjustable-focus endoscope with a solid electrically tunable lens. *Optics Express* **23**, 20582-20592, doi:10.1364/oe.23.020582 (2015).
- 3 Barbero, S. & Rubinstein, J. Adjustable-focus lenses based on the Alvarez principle. *Journal of Optics* **13**, doi:10.1088/2040-8978/13/12/125705 (2011).
- 4 Lou, Y., Chen, L., Wang, C. & Shen, S. Tunable-focus liquid crystal Fresnel zone lens based on harmonic diffraction. *Applied Physics Letters* **101**, doi:10.1063/1.4769090 (2012).
- 5 Valley, P. *et al.* Tunable-focus flat liquid-crystal diffractive lens. *Optics Letters* **35**, 336-338, doi:10.1364/ol.35.000336 (2010).
- 6 Lin, Y.-H., Wang, Y.-J. & Reshetnyak, V. Liquid crystal lenses with tunable focal length. *Liquid Crystals Reviews* **5**, 111-143, doi:10.1080/21680396.2018.1440256 (2017).
- 7 Wang, B., Ye, M., Honma, M., Nose, T. & Sato, S. Liquid crystal lens with spherical electrode. *Japanese Journal of Applied Physics Part 2-Letters* **41**, L1232-L1233, doi:10.1143/jjap.41.L1232 (2002).
- 8 Lin, H.-C. & Lin, Y.-H. An electrically tunable-focusing liquid crystal lens with a low voltage and simple electrodes. *Optics Express* **20**, 2045-2052, doi:10.1364/oe.20.002045 (2012).
- 9 Pishnyak, O., Sato, S. & Lavrentovich, O. D. Electrically tunable lens based on a dual-frequency nematic liquid crystal. *Applied Optics* **45**, 4576-4582, doi:10.1364/ao.45.004576 (2006).
- 10 Dong, L., Agarwal, A. K., Beebe, D. J. & Jiang, H. Adaptive liquid microlenses activated by stimuli-responsive hydrogels. *Nature* **442**, 551-554, doi:10.1038/nature05024 (2006).
- 11 Lopez, C. A. & Hirs, A. H. Fast focusing using a pinned-contact oscillating liquid lens. *Nature Photonics* **2**, 610-613, doi:10.1038/nphoton.2008.198 (2008).
- 12 Hasan, N., Kim, H. & Mastrangelo, C. H. Large aperture tunable-focus liquid lens using shape memory alloy spring. *Optics Express* **24**, 13334-13342, doi:10.1364/oe.24.013334 (2016).
- 13 Carpi, F., Frediani, G., Turco, S. & De Rossi, D. Bioinspired Tunable Lens with Muscle-Like Electroactive Elastomers. *Advanced Functional Materials* **21**, 4152-4158, doi:10.1002/adfm.201101253 (2011).
- 14 Maffli, L., Rosset, S., Ghilardi, M., Carpi, F. & Shea, H. Ultrafast All-Polymer Electrically Tunable Silicone Lenses. *Advanced Functional Materials* **25**, 1656-1665, doi:10.1002/adfm.201403942 (2015).
- 15 Wang, S. *et al.* A broadband achromatic metalens in the visible. *Nature Nanotechnology* **13**, 227-232, doi:10.1038/s41565-017-0052-4 (2018).
- 16 Chen, W. T. *et al.* A broadband achromatic metalens for focusing and imaging in the visible. *Nature Nanotechnology* **13**, 220+, doi:10.1038/s41565-017-0034-6 (2018).
- 17 Arbabi, A. *et al.* Miniature optical planar camera based on a wide-angle metasurface doublet corrected for monochromatic aberrations. *Nature Communications* **7**, doi:10.1038/ncomms13682 (2016).

- 18 Paniagua-Dominguez, R. *et al.* A Metalens with a Near-Unity Numerical Aperture. *Nano Letters* **18**, 2124-2132, doi:10.1021/acs.nanolett.8b00368 (2018).
- 19 Guo, Y. *et al.* High-Efficiency and Wide-Angle Beam Steering Based on Catenary Optical Fields in Ultrathin Metalens. *Advanced Optical Materials* **6**, doi:10.1002/adom.201800592 (2018).
- 20 Liang, H. *et al.* High performance metalenses: numerical aperture, aberrations, chromaticity, and trade-offs. *Optica* **6**, 1461-1470, doi:10.1364/optica.6.001461 (2019).
- 21 Ni, X., Kildishev, A. V. & Shalaev, V. M. Metasurface holograms for visible light. *Nature Communications* **4**, doi:10.1038/ncomms3807 (2013).
- 22 Wen, D. *et al.* Helicity multiplexed broadband metasurface holograms. *Nature Communications* **6**, doi:10.1038/ncomms9241 (2015).
- 23 Huang, L. *et al.* Three-dimensional optical holography using a plasmonic metasurface. *Nature Communications* **4**, doi:10.1038/ncomms3808 (2013).
- 24 Huang, L., Zhang, S. & Zentgraf, T. Metasurface holography: from fundamentals to applications. *Nanophotonics* **7**, 1169-1190, doi:10.1515/nanoph-2017-0118 (2018).
- 25 Zhao, R. *et al.* Multichannel vectorial holographic display and encryption. *Light-Science & Applications* **7**, doi:10.1038/s41377-018-0091-0 (2018).
- 26 Basiri, A. *et al.* Nature-inspired chiral metasurfaces for circular polarization detection and full-Stokes polarimetric measurements. *Light-Science & Applications* **8**, doi:10.1038/s41377-019-0184-4 (2019).
- 27 Rubin, N. A. *et al.* Matrix Fourier optics enables a compact full-Stokes polarization camera. *Science* **365**, 43-+, doi:10.1126/science.aax1839 (2019).
- 28 Yang, Z. *et al.* Generalized Hartmann-Shack array of dielectric metalens sub-arrays for polarimetric beam profiling. *Nature Communications* **9**, doi:10.1038/s41467-018-07056-6 (2018).
- 29 Wu, P. C. *et al.* Visible Metasurfaces for On-Chip Polarimetry. *Acs Photonics* **5**, 2568-2573, doi:10.1021/acsp Photonics.7b01527 (2018).
- 30 Devlin, R. C., Ambrosio, A., Rubin, N. A., Mueller, J. P. B. & Capasso, F. Arbitrary spin-to-orbital angular momentum conversion of light. *Science* **358**, 896-900, doi:10.1126/science.aao5392 (2017).
- 31 Fan, Q. *et al.* Broadband Generation of Photonic Spin-Controlled Arbitrary Accelerating Light Beams in the Visible. *Nano Letters* **19**, 1158-1165, doi:10.1021/acs.nanolett.8b04571 (2019).
- 32 Huang, L. *et al.* Volumetric Generation of Optical Vortices with Metasurfaces. *Acs Photonics* **4**, 338-346, doi:10.1021/acsp Photonics.6b00808 (2017).
- 33 Li, Z., Cheng, H., Liu, Z., Chen, S. & Tian, J. Plasmonic Airy Beam Generation by Both Phase and Amplitude Modulation with Metasurfaces. *Advanced Optical Materials* **4**, 1230-1235, doi:10.1002/adom.201600108 (2016).
- 34 Zeng, B. *et al.* Hybrid graphene metasurfaces for high-speed mid-infrared light modulation and single-pixel imaging. *Light-Science & Applications* **7**, doi:10.1038/s41377-018-0055-4 (2018).
- 35 Li, S.-Q. *et al.* Phase-only transmissive spatial light modulator based on tunable dielectric metasurface. *Science* **364**, 1087-+, doi:10.1126/science.aaw6747 (2019).
- 36 Zou, C. *et al.* Electrically Tunable Transparent Displays for Visible Light Based on Dielectric Metasurfaces. *Acs Photonics* **6**, 1533-1540, doi:10.1021/acsp Photonics.9b00301 (2019).

- 37 Dai, J. Y., Zhao, J., Cheng, Q. & Cui, T. J. Independent control of harmonic amplitudes and phases via a time-domain digital coding metasurface. *Light-Science & Applications* **7**, doi:10.1038/s41377-018-0092-z (2018).
- 38 Arbabi, E. *et al.* MEMS-tunable dielectric metasurface lens. *Nature Communications* **9**, doi:10.1038/s41467-018-03155-6 (2018).
- 39 Callewaert, F. *et al.* Inverse-designed stretchable metalens with tunable focal distance. *Applied Physics Letters* **112**, doi:10.1063/1.5017719 (2018).
- 40 Kamali, S. M., Arbabi, E., Arbabi, A., Horie, Y. & Faraon, A. Highly tunable elastic dielectric metasurface lenses. *Laser & Photonics Reviews* **10**, 1002-1008, doi:10.1002/lpor.201600144 (2016).
- 41 She, A., Zhang, S., Shian, S., Clarke, D. R. & Capasso, F. Adaptive metalenses with simultaneous electrical control of focal length, astigmatism, and shift. *Science Advances* **4**, doi:10.1126/sciadv.aap9957 (2018).
- 42 Afridi, A. *et al.* Electrically Driven Varifocal Silicon Metalens. *Acs Photonics* **5**, 4497-+, doi:10.1021/acsp Photonics.8b00948 (2018).
- 43 Colburn, S., Zhan, A. & Majumdar, A. Varifocal zoom imaging with large area focal length adjustable metalenses. *Optica* **5**, 825-831, doi:10.1364/optica.5.000825 (2018).
- 44 Aiello, M. D. *et al.* Achromatic Varifocal Metalens for the Visible Spectrum. *Acs Photonics* **6**, 2432-2440, doi:10.1021/acsp Photonics.9b00523 (2019).
- 45 Yamada, K., Watanabe, W., Li, Y. D., Itoh, K. & Nishii, J. Multilevel phase-type diffractive lenses in silica glass induced by filamentation of femtosecond laser pulses. *Optics Letters* **29**, 1846-1848, doi:10.1364/ol.29.001846 (2004).

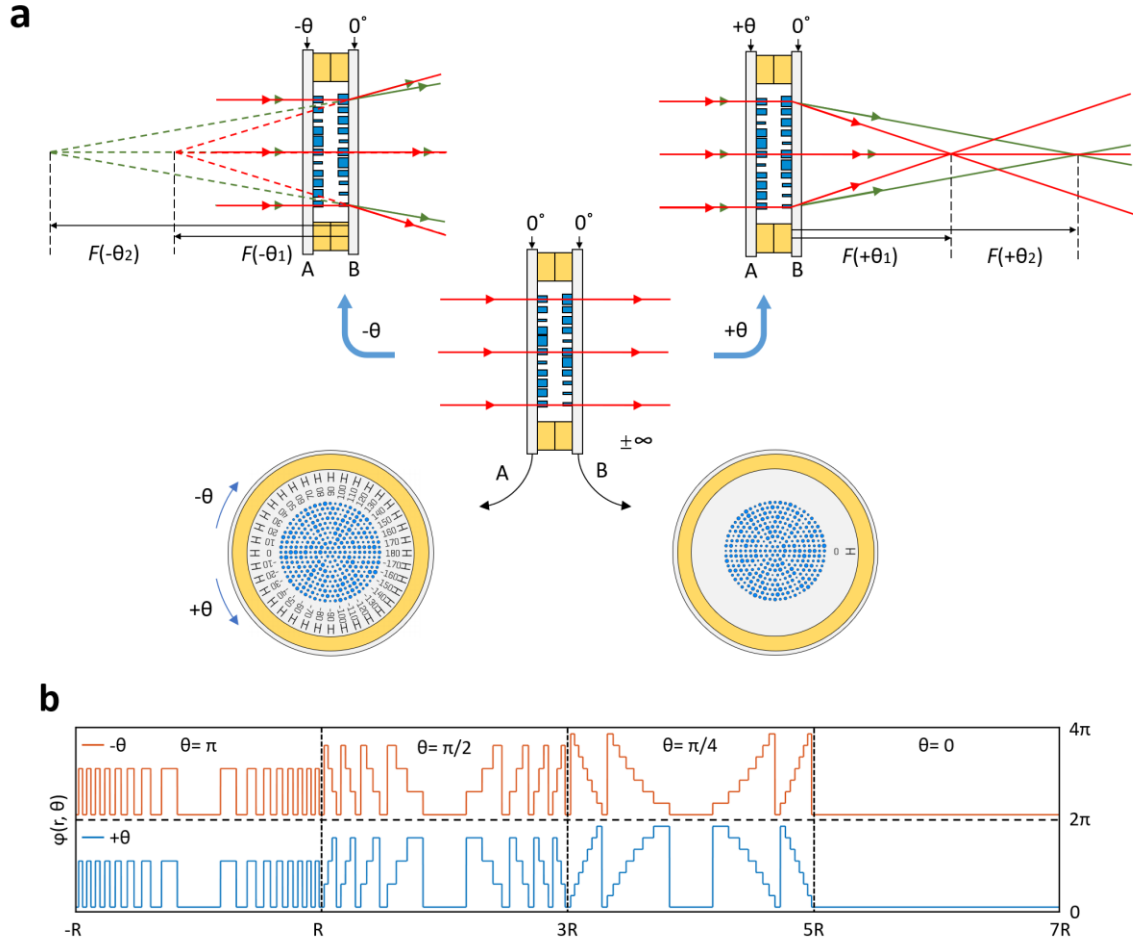


**Fig.1 | Illustration of the metasurface doublet and designed wavefront output. a**, Schematic illustration of the zooming imaging doublet consisted of two metasurfaces. With different rotation angle  $\theta$  of one metasurface, the focal length of the doublet changes continuously. When rotating in the positive direction  $+\theta$ , the doublet works as a positive lens, whereas as a negative lens in  $-\theta$ . The mark 'H' is carved for alignment. **b**, The output phase profile of the doublet in different angle. The phase is quantitative, and the quantitation level varies when the angle is adjusted. Respectively, the quantitative level  $n$  is  $n=2$  when the rotation angle  $\theta=\pm\pi$ ,  $n=4$  when  $\theta=\pm\pi/2$ ,  $n=8$  when  $\theta=\pm\pi/4$ , and  $n=\infty$  when  $\theta=\pm 0$ .

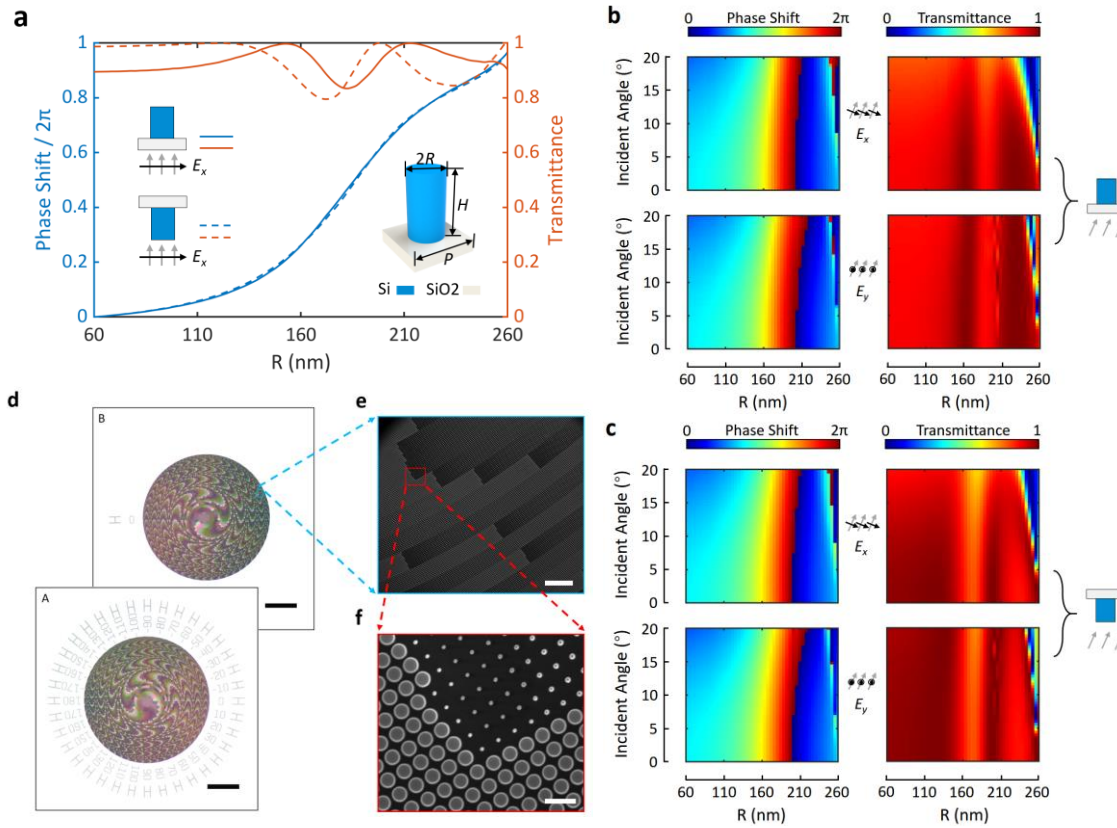


**Fig.2 | Design of the unit nano scatter and images of the optical and scanning electron micrography.** **a**, Simulated phase shift and transmittance of a single nano scatter with different sides of linearly x-polarized normal incidences and the chematic of the unit nano scatter lattice. The simulation results with the incidence from the bottom are plotted with solid lines, and those with the incident from the top are with dash lines. The scatter comprises a Si nanopillar with varying radius  $R$  but equal height  $H=700$  nm and a SiO<sub>2</sub> square base with a constant width  $P=600$  nm. **b**, Simulated phase shift and transmittance of a single nano scatter with differetn incident angles when the incidence injects from the bottom. The upper two images are the simulated results under x-linear polarized light, and the lower two ones are uner linearly y-polarized light. **c**, Simulated phase shift and transmittance of a single nano scatter with differetn incident angles when the incidence injects from the top. The upper two images are the simulated results under linearly x-polarized light, and the lower two ones are uner linearly y-polarized light. **d**, Optical micrography of two whole fabricated metasurfaces. Scale bare:  $250$   $\mu\text{m}$ . **e**, Scanning electron micrography of the bule rectangle marked area in **d**. Scale bar:  $7.5$   $\mu\text{m}$ . **f**, Scanning electron micrography of the red rectangle marked area in **e**. Scale bar:  $1$   $\mu\text{m}$ .

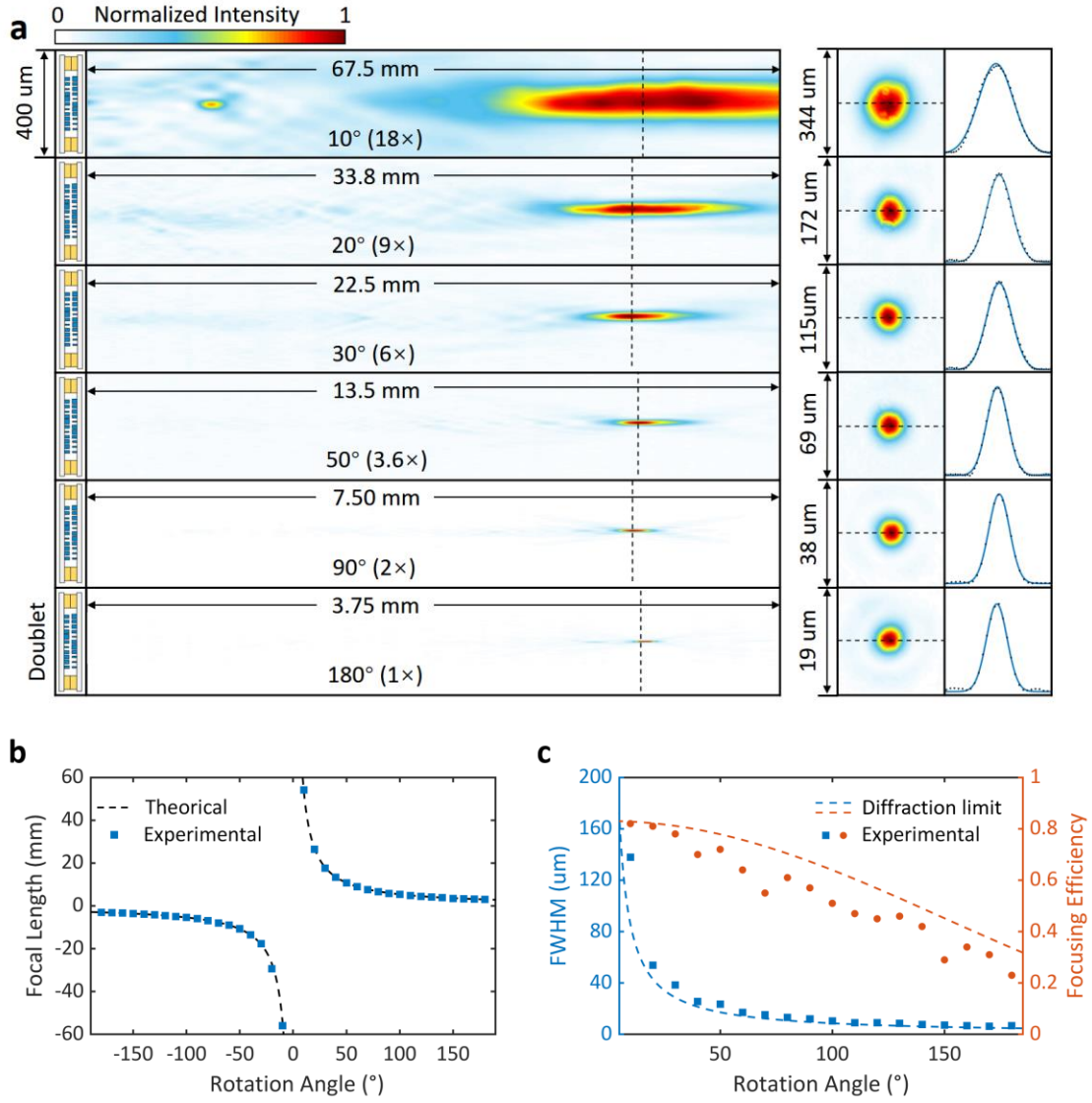


**Fig.3 | Measured focusing behaviors and corresponding key properties of the doublet. a,** Normalized intensity distributions of the focal field along the optical axis and in the focal plane under six rotation angles. The total zoom range is 18x. Positions of black dash lines in the images along optical axes are chosen as focal planes. Intensity values along dash lines in the images of focal planes are plotted as cross profiles of focal spots and fitted with the gaussian function. Widths of images along optical axes are set according to the designed zoom power. Sizes of images of focal planes are set as 4x of diffraction limits of corresponding theoretical NAs. **b,** Theoretical and experimental results of focal lengths under different angles for both positive and negative lens modes. **c,** FWHMs and focusing efficiencies under different angles for positive lens mode. Theoretical values are plotted in dash lines, and measured values are plotted in square and circle points in **b, c**.



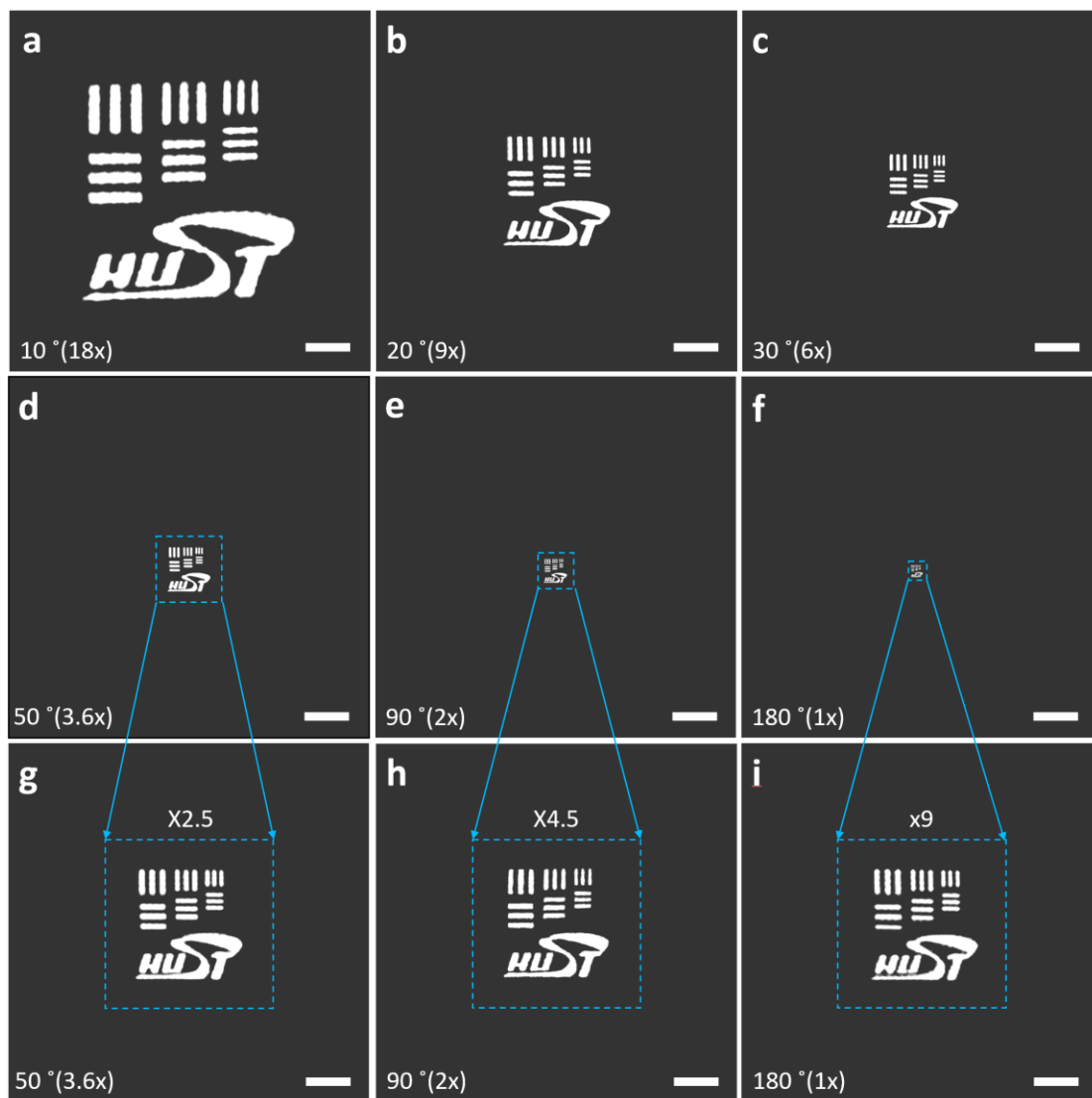


**Fig.4 | Captured zooming images with the  $4f$  system comprising the doublet and a conventional lens. a-f,** Images of the fabricated resolution target under six rotation angles. The total zoom range is 18x. Scale bar: 1 mm. **g-i,** Magnifications of images under the rotation angle of  $50^\circ$ ,  $90^\circ$  and  $180^\circ$ . The magnified power  $N$  is set following the equation  $Nk=9$ , where  $k$  is the designed zoom power under corresponding rotation angle. Scale bar: 400  $\mu\text{m}$  in **g**, 222  $\mu\text{m}$  in **h** and 111  $\mu\text{m}$  in **i**.